AGU PUBLICATIONS

JGR

Journal of Geophysical Research: Space Physics

RESEARCH ARTICLE

10.1002/2017JA024708

**Key Points:**
- Plasmapause location is stable before, during, and after this substorm over wide range of MLT
- There are multiple intensifications of a plasmaspheric virtual resonance (PVR) with spatially varying amplitude
- PVR wave frequency remains stable at 8.2 ± 0.53 mHz during 2 h period despite changing magnetospheric and ionospheric conditions

**Correspondence to:**
M. D. Hartinger,
mdhartin@vt.edu

**Citation:**
Hartinger, M. D., Zou, S., Takahashi, K., Shi, X., Redmon, R., Goldstein, J., … Bonnell, J. W. (2017). Nightside Pi2 wave properties during an extended period with stable plasmapause location and variable geomagnetic activity. *Journal of Geophysical Research: Space Physics*, *122*, 12,120–12,139. https://doi.org/10.1002/2017JA024708

Received 24 AUG 2017
Accepted 10 NOV 2017
Accepted article online 13 NOV 2017
Published online 11 DEC 2017



# Nightside Pi2 Wave Properties During an Extended Period With Stable Plasmapause Location and Variable Geomagnetic Activity

**M. D. Hartinger[1], S. Zou[2], K. Takahashi[3], X. Shi[1], R. Redmon[4], J. Goldstein[5], W. Kurth[6], and J. W. Bonnell[7]**

[1]Department of Electrical and Computer Engineering, Virginia Polytechnic Institute and State University, Blacksburg, VA, USA, [2]Department of Climate and Space Science and Engineering, University of Michigan, Ann Arbor, MI, USA, [3]Applied Physics Laboratory, The Johns Hopkins University, Laurel, MD, USA, [4]National Oceanic and Atmospheric Administration, Boulder, CO, USA, [5]Southwest Research Institute, San Antonio, TX, USA, [6]Department of Physics and Astronomy, University of Iowa, Iowa City, IA, USA, [7]Space Science Laboratory, University of California, Berkeley, CA, USA

**Abstract** The frequencies and amplitudes of inner magnetosphere Pi2 waves are affected by the radial plasma density profile. Variable geomagnetic activity and external driving conditions can affect both wave properties and density profiles simultaneously. When interpreting observations, this can lead to ambiguity about whether changing wave properties are due to changing external conditions, density profiles, or a combination of factors. We present a case study using multipoint ground-based and in situ measurements to examine Pi2 wave properties during a period of variable geomagnetic activity. Multiple satellite passes demonstrate the density profile and plasmapause location are stable for at least 2 h over a wide range of magnetic local time. This stability allows us to examine how factors besides the radial density profile affect Pi2 wave properties. We find evidence for Pi2 waves with a broadband frequency spectrum as well as a discrete frequency plasmaspheric virtual resonance (PVR) that is observed at low, middle, and high latitudes and both inside and outside the plasmapause. The PVR is excited in repeated bursts before, during, and after (1) the development of a substorm, (2) several auroral intensifications, (3) the development of Subauroral Polarization Stream flows/electric fields/conductivities, and (4) variable interplanetary magnetic field conditions. Through all these changes the PVR frequency remains remarkably stable (8.2 ± 0.53 mHz, based on low-latitude ground magnetometer observations), suggesting that these variations have little effect on the frequency. This is consistent with PVR model predictions for a stationary plasmapause.

## 1. Introduction

Ultralow frequency (ULF) waves in the Earth's magnetosphere are classified according to their frequencies and durations (Jacobs et al., 1964). Pi2 waves have periods of 40–150 s (7–25 mHz) and occur during events lasting roughly 10–15 min; they are primarily a nightside phenomena (Keiling & Takahashi, 2011). Models of Pi2 waves often describe wave dynamics using a magnetohydrodynamic (MHD) approximation (e.g., Fujita & Tanaka, 2013; Lee & Kim, 1999; Lysak et al., 2015; Ream et al., 2015).

Models and observations show that many ULF wave modes are strongly affected by the radial Alfvén speed profile (e.g., Archer et al., 2015, 2017; Hartinger et al., 2010; Kivelson et al., 1984). In the inner magnetosphere, variations in the total magnetic field are often small compared to background values, while density variations can be significant; thus, when considering Alfvén speed variations and ULF wave properties in the inner magnetosphere, constraining the radial density profile is crucial.

The plasmasphere—a region of cold, dense plasma in the inner magnetosphere—often creates conditions favorable for the trapping of MHD wave energy. Several Pi2 models predict eigenmodes similar to radially standing MHD fast mode waves with frequencies primarily determined by the radial density and Alfvén speed profiles (e.g., Lee & Kim, 1999). For example, plasmaspheric virtual resonances (PVR) have similar polarizations to radially standing fast mode waves (i.e., azimuthal electric field and field-aligned magnetic field 90° out of phase), radially distributed nodes and antinodes, and stable frequencies over a wide range of

latitudes (*L* values) and longitudes. In many cases, signals measured at widely separated latitudes and longitudes exhibit little or no phase shift, indicating globally coherent wave activity with very small azimuthal wave numbers (Li et al., 1998; Nosé et al., 2008). PVR can also have finite wave amplitudes both inside and outside the plasmasphere (Lee & Kim, 1999). Observational studies have confirmed the existence of PVR, and they have frequencies in the Pi2 range (Ghamry et al., 2015; Luo et al., 2011; Nosé, 2010; Shi et al., 2017; Takahashi et al., 2009; Teramoto et al., 2011); they may also be classified as Pc4 waves (e.g., Takahashi et al., 2005).

Multiple factors affect inner magnetosphere Pi2 wave frequencies, particularly during geomagnetically active conditions. During the course of a substorm, sources for Pi2 wave frequencies may include Bursty Bulk Flows (BBFs) (Kepko et al., 2001), PVR (Lee & Kim, 1999), Alfvén waves standing along the magnetic field, plasmapause surface waves, and other mechanisms (Keiling & Takahashi, 2011). Each mechanism has a unique frequency dependence on plasma mass density, ionospheric conductivity, and other factors that can change with time during the substorm. Thus, one may not expect observed Pi2 wave frequencies to remain stable before, during, and after a substorm or during other geomagnetically active periods.

For example, the plasmasphere is generally expected to erode during substorms and periods with southward Interplanetary Magnetic Field (IMF). Though erosion may not occur on timescales comparable to Pi2 event timescales, substantial erosion may well occur between Pi2 events altering the Pi2 wave frequency from one event to the next. At the same time ionospheric parameters such as density and conductivity may change rapidly associated with the development of Sub-Auroral Polarization Streams (SAPS) (Anderson et al., 1993). SAPS are large, westward ionospheric flows observed during geomagnetically active periods with peak flow speeds equatorward of the electron plasma sheet (energies on the order of 1 keV) precipitation boundary (Foster & Vo, 2002). Ionospheric density and conductivity variations due to SAPS and other phenomena may also affect the properties of Pi2 waves (e.g., Ream et al., 2015).

The interpretation of observations in the context of one or more Pi2 wave models is complicated by uncertainty about whether changing wave properties are due to changing external conditions, density profiles, or a combination of the two. This study addresses this complication by examining a 2 h period with stationary plasmapause and variable geomagnetic activity. This is made possible by a favorable satellite conjunction: (1) multiple plasmapause crossings in the premidnight sector made by probes on similar orbits, (2) multiple plasmapause crossings in the predawn sector made by probes on similar orbits, and (3) crossings overlap the region of wave activity and substorm/SAPS activity, both spatially and temporally. As we shall show, a discrete frequency PVR is excited multiple times with a stable frequency before, during, and after a substorm. The substorm and other geomagnetic activity have no effect on the PVR frequency due to the stationary plasmapause, though they affect the spatial and temporal variation of wave amplitude.

## 2. Instrumentation and Signal Processing

In situ measurements of ULF waves and electron density are obtained from the Van Allen Probes mission (also referred to as Radiation Belt Storm Probes, or RBSP). RBSP is a two-satellite constellation designed to study many aspects of radiation belt dynamics (Mauk et al., 2012). These probes have low-inclination, elliptical orbits with geocentric apogee near 5.8 $R_E$ and nominal spin periods of roughly 11 s. The spin axis nominally points toward the Sun. We use the Electric and Magnetic Field Instrument Suite and Integrated Science (EMFISIS) (Kletzing et al., 2013) high-frequency plasma wave measurement (measurements of a single electric field component from 10 to 500 kHz) to determine the upper hybrid frequency and infer the electron density using the technique discussed by Kurth et al. (2015). For ULF wave measurements, we examine spinfit electric fields using the RBSP Electric Field and Waves instrument (EFW) (Wygant et al., 2013) spin plane booms. For the intervals examined in this study, the angle between the spin axis and the background magnetic field is typically larger than 80°, so it is not generally possible to obtain the spin axis component of the electric field using the $\vec{E} \cdot \vec{B} = 0$ approximation. We examined the electric field measured directly by the spin axis boom, but it is affected by contamination in the DC and ULF frequency ranges due to its short length/proximity to spacecraft. Additionally, the DC/ULF electric field from the spin axis boom measurement and $\vec{E} \cdot \vec{B} = 0$ do not agree during the period of interest. Thus, we shall focus solely on the two spin plane measurements.

In addition to RBSP, we use Geostationary Operational Environmental Satellites (GOES) and Time History of Events and Macroscale Interactions during Substorms (THEMIS) satellites for in situ measurements of ULF waves, particle injections, and densities at larger L shell. In particular, we use GOES satellite fluxgate

**Table 1**
*Ground Magnetometer Locations in Geographic and Corrected Geomagnetic (CGM) Coordinates*

| Station | Name | Geo latitude | Geo longitude | CGM latitude | CGM longitude |
|---|---|---|---|---|---|
| PGEO | Prince George | 53.82 | 237.2 | 59.04 | 297.0 |
| UKIA | Ukiah | 45.14 | 241.1 | 51.15 | 304.0 |
| CCNV | Carson City | 39.19 | 240.2 | 44.99 | 304.5 |
| FTN | Fort Nelson | 58.90 | 237.2 | 64.09 | 295.1 |
| FSJ | Fort Saint John | 56.20 | 239.1 | 61.80 | 298.4 |
| VIC | Victoria | 48.52 | 236.6 | 53.61 | 298.0 |
| FRN | Fresno | 37.09 | 240.3 | 42.89 | 305.1 |
| BSL | Stennis | 30.35 | 270.4 | 40.73 | 342.1 |
| FRD | Fredericksburg | 38.20 | 282.6 | 48.04 | 359.4 |
| FSIM | Fort Simpson | 61.76 | 238.8 | 67.18 | 295.6 |

*Note.* PGEO, UKIA, and CCNV are from the THEMIS array. FTN and FSJ are from the STEP array. VIC is from the CANMON array. FRN, BSL, and FRD are from the USGS array. FSIM is from the CARISMA array. Geographic coordinates were obtained from the respective array Web sites or instrument papers, while CGM coordinates were obtained using the NASA Virtual Ionosphere, Thermosphere, Mesosphere Observatory via the online OMNIWeb interface by specifying each station's geographic position, the 2010 version of the IGRF model modified slightly with predictive terms appropriate for 2013, and an altitude of 0 km. These coordinates may differ slightly from those reported elsewhere when using a different version of IGRF. Figure 3 shows the map of geographic locations.

magnetometers (Singer et al., 1996) and electron detectors (Onsager et al., 1996), specifically the magnetospheric electron detector (MAGED) telescope mounted at 0° from the anti-earthward direction (Redmon et al., 2015; Rodriguez, 2014), though other MAGED detectors yield qualitatively similar results for the purpose of this study. We also use observations of spacecraft potential from the THEMIS satellites, which can be used to infer electron density (McFadden et al., 2008; Sibeck & Angelopoulos, 2008).

For ground-based wave observations, we use magnetometer data from the THEMIS ground-based network (Russell et al., 2008), Canadian Array for Realtime InvestigationS of Magnetic Activity (CARISMA) (Mann et al., 2008), Canadian Magnetic Observatory Network (CANMON), Solar-Terrestrial Energy Program (STEP) polar network, and United States Geological Survey (USGS) (Love & Finn, 2011). Table 1 shows the magnetic and geographic coordinates of each station. Data links with additional information about these stations are provided in the Acknowledgments section.

For additional context on overall geomagnetic activity, ionospheric plasma flows, and wave activity, we use geomagnetic activity indices and propagated solar wind observations, all-sky imagers, and midlatitude high-frequency radars in the Super Dual Auroral Radar Network (SuperDARN). Geomagnetic activity indices and solar wind observations (propagated to the Earth's bow shock) are obtained from the NASA Space Physics Data Facility OMNIWeb interface at http://omniweb.gsfc.nasa.gov. All-sky imager (ASI) observations are taken from the Fort Simpson (FSIM), Fort Smith (FSMI), Gillam (GILL), Fort Yukon (FYKN), and Sanikiluaq (SNKQ) stations in the THEMIS array via the public THEMIS database (Mende et al., 2008). SuperDARN measurements are taken from a public database at Virginia Tech. These radars measure the line-of-sight (LOS) velocity component of the ionospheric plasma drift in the *F* region. Multiple radars can be used together to derive global maps of the electric potential and flow patterns in the ionosphere using standard tools available on the Virginia Tech Web site (Ruohoniemi & Baker, 1998). Most radars operate in a mode that sweeps the radar field of view every 1–2 min. However, special modes are available at higher resolution. In this study, we show measurements from the Fort Hays West (FHW) and Christmas Valley East (CVE) radars when operating in the RBSP mode, with select beams sampling at 19 s cadence.

For wave analysis in the frequency domain, we examine dynamic power spectra of the magnetic and electric field, where all signals are first interpolated to have the same 11 s time resolution (the lowest resolution across all measurements that were analyzed in the frequency domain) using the nearest neighbor technique. Throughout the manuscript, dynamic power spectra are obtained using a running 128 point (23.5 min) Discrete Fourier Transform (DFT) with 94% window overlap. Prior to taking the DFT, a line is fit to the data in the

23.5 min window and subtracted from the original data to obtain perturbation fields, and a Hanning window is applied to reduce spectral leakage. The power spectrum is then computed using a three-point smooth over frequency to improve the signal-to-noise ratio of the coherent ULF pulsation over the incoherent background noise. In Figures 6 and 9 we also examine normalized dynamic power spectra to focus on the time evolution of spectral features; these are obtained by dividing the power in each frequency bin by the maximum power in the 5–20 mHz frequency band at each time step. Finally, in Figure 6 (ninth panel) and Figure 7 (bottom right), we high-pass filter time series using a 5 mHz cutoff to more easily examine amplitude and phase differences between signals.

The DFT frequency bin width is 2.13 mHz when using the 128-point window and three-point smoothing. Thus, when we identify frequencies based on a power spectrum peak, there is an uncertainty of roughly ±1.1 mHz. To better assess the wave frequency stability, we use a longer 256-point DFT window with three-point smoothing in Figure 6 (eighth panel), increasing the frequency resolution by a factor of 2 at the expense of capturing some temporal variations. Generally, when we refer to a discrete frequency of 8 mHz in this study, it should be understood that there is some uncertainty in the frequency determination, either ±1.1 mHz or ±0.53 mHz depending on the DFT window length and that the peak frequency may vary slightly depending on the choice of DFT window length and amount of smoothing in frequency domain. For example, the frequency bin with peak PVR power is 7.8 mHz when using the 128-point window with three-point smooth, while it is 8.2 mHz when using the 256-point window with three-point smooth. To avoid confusion, we simply refer to this as an 8 mHz signal throughout. The only exception occurs when discussing the stability of the PVR frequency; in that discussion, we shall directly reference this uncertainty as 8.2 mHz ±0.53 mHz, based on the lower and upper bounds of the frequency bin corresponding to the power spectrum peak observed by low-latitude ground magnetometers, when using the 256-point DFT window.

Finally, we note that when comparing dynamic power spectra constructed using the interpolated 11 s ground magnetometer time series and the original 1 s time series, there were no significant differences in the frequency band of interest, 5–20 mHz. This suggests that 11 s samples (Nyquist frequency 45 mHz) are sufficient to capture the wave activity of interest.

## 3. Observations

### 3.1. Solar Wind and Geomagnetic Activity Overview

The ULF wave event occurred on 16 March 2013, with the period of interest 0630–0830 UT. Figure 1 shows an overview of the interplanetary magnetic field (IMF) and geomagnetic activity during 0000–0900 UT, with the interval of interest for Pi2 wave activity marked by pink lines. Figure 1 (first panel) shows the time-shifted (to bow shock nose) IMF measurement in GSM coordinates from OMNIWeb. The IMF is southward for much of the day, but it turns northward at 0630 UT. A southward turning of the IMF occurs between 0700 and 0710 UT, after which the *z* component remains negative for roughly the next 40 min. During this period, the solar wind flow speed and dynamic pressure (not shown) are mostly steady at roughly 450 km/s and 1.7 nPa, respectively. There are some small variations in speed and pressure prior to 0700 UT, though these do not appear to have a direct impact on Pi2 wave properties in the magnetosphere thus will not be discussed further.

Figure 1 (second panel) is for the *AL* index obtained from OMNIWeb. For much of the early part of the day, *AL* is below −200 nT with several sharp decreases to lower values, such as the period just before 0400 UT. At the beginning of the 0630–0830 UT period of interest, *AL* is closer to 0 indicating quiet conditions. A rapid decrease in *AL* at 0720 UT is associated with substorm activity, with substorm onset at 0716 UT within the THEMIS FSIM ASI field of view (Figure 1, fourth panel). This is consistent with energetic electron measurements from the GOES 15 satellite. In particular, differential electron fluxes from the GOES 15 MAGED detector oriented at 0° from the anti-earthward direction are shown in Figure 1 (third panel) with energy labels corresponding to the center energies of different channels. These data indicate that GOES 15, located at geostationary orbit near 22 magnetic local time (MLT), observes an electron injection at the onset time; note that the other GOES 15 MAGED telescopes as well as GOES 15 proton detectors observe the same injection timing and qualitatively similar results for the purpose of this study (not shown). Finally, the rapid decrease in *AL* is also consistent with the keogram generated using measurements from the FSIM ASI in Figure 1 (fourth panel); FSIM is at a similar MLT as the GOES spacecraft, and it observes the westward traveling surge about 1 min after the initial onset at FSIM (see Figure 6 (second panel) for more details with shorter time range).

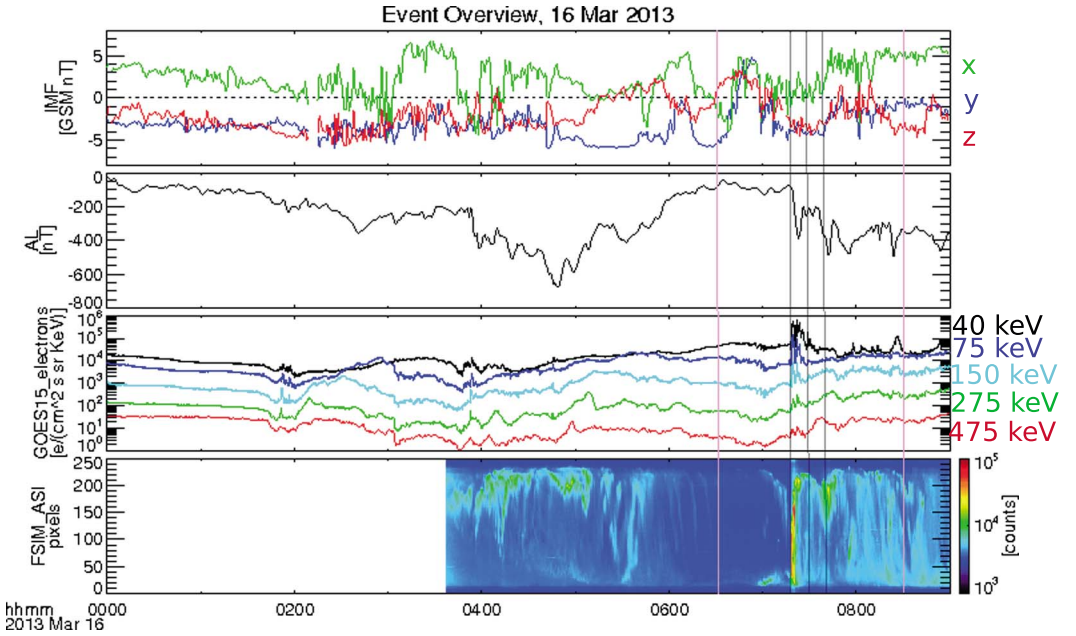


**Figure 1.** From top to bottom, (first panel) OMNIWeb interplanetary magnetic field in GSM coordinates and propagated from measurement location to the Earth's bow shock, (second panel) *AL* index, (third panel) electron energy flux measurements from GOES 15 MAGED detector oriented at 0° from the anti-earthward direction with different energy channels center energies indicated by color, (fourth panel) Fort Simpson (FSIM) all-sky imager keogram showing intensity in color. Two pink lines indicate the interval of interest for Pi2 wave activity, while three gray lines indicate times corresponding to flow patterns shown in Figure 2.

Figure 2 shows ionospheric flows associated with the substorm activity at 0720, 0730, and 0740 UT (times indicated in Figure 1 by gray lines). Flow directions are indicated by dots and lines where the base of the vector is the dot, and velocity magnitude is indicated by both color and the length of the line. These figures were generated by a spherical harmonic regression mapping procedure using LOS velocity measurements from all the SuperDARN radars in the Northern Hemisphere (Ruohoniemi & Baker, 1998). A large, westward directed flow develops at 0720 UT near 21–22 MLT, as indicated by the flow pattern in Figure 2 (top). It intensifies by 0730, with flows reaching 800 km/s, as indicated by the flow pattern in Figure 2 (middle). The region with the large westward flow also spreads eastward. Finally, the flow pattern at 0740 UT (Figure 2, bottom) indicates that the region with large flows continues to spread eastward, but the flows begin to weaken.

In summary, Figure 1 indicates southward IMF and several sharp decreases in *AL* for much of the early part of the day, then relatively quiet conditions in the nightside magnetosphere at the beginning of the interval of interest, 0630 UT, until roughly 0716 UT when a substorm occurs. Following this, a region of large, westward flow intensifies and spreads in the midlatitude ionosphere, as shown in Figure 2. These observations are consistent with the definition of SAPS (Foster & Vo, 2002) and the SAPS evolution after substorm onset (Zou et al., 2012; Zou, Lyons, Nicolls, et al., 2009; Zou, Lyons, Wang, et al., 2009). Zou, Lyons, Wang, et al. (2009) and Zou, Lyons, Nicolls, et al. (2009) showed that SAPS increased equatorward of the auroral onset as a consequence of field-aligned current closure. In this case, auroral onset is initiated close to FSIM, with SAPS initially developing equatorward of FSIM and spreading eastward at later times.

### 3.2. Plasmapause Location

In this section we identify the location of the plasmapause in electron density data and show where in situ and ground-based observations are located relative to the plasmapause. Figure 3a is for the satellite orbits in the GSM *xy* plane from 06:30 to 08:30 UT. Figure 3b is for the ground station positions (green diamonds) and locations of SuperDARN beams that will be analyzed in a later figure (white lines). Using the IGRF model combined with the Tsyganenko (1989) external magnetic field model (results are similar when using other external models), we map nightside satellite locations from the magnetosphere to the ground: RBSP-A (pink crosses), RBSP-B (black crosses), GOES 13 (light blue diamond), and GOES 15 (dark blue diamond). For global context a solid green line indicates the plasmapause location at $L \sim 4.4R_E$, determined using analysis in the

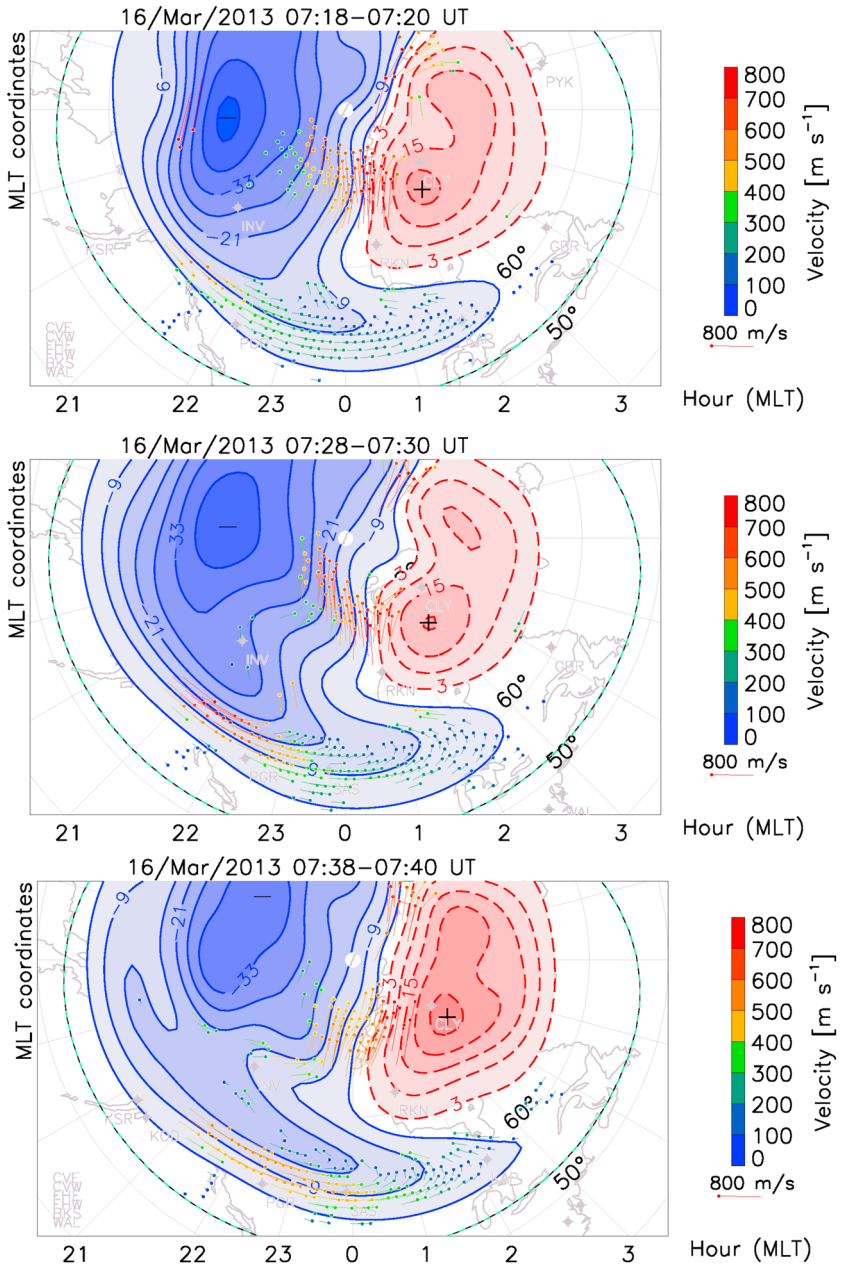


**Figure 2.** Global maps of the ionospheric electric potential and flow pattern derived from fits to measurements from multiple SuperDARN radars at (top) 0720 UT, (middle) 0730 UT, and (bottom) 0740 UT (times indicated by gray lines in Figure 1).

next figure. Additional context is provided by all-sky images taken from FYKN, FSIM, FSMI, GILL, and SNKQ at 0718 UT, that is, roughly 2 min after the substorm onset; these show the location of a large auroral arc associated with the substorm mentioned in the previous section (note that midlatitude stations in North America were affected by cloud cover during this event). Finally, LOS velocities measured using the FHW SuperDARN radar are shown in color, also from 0718 UT. Larger flows are generally seen adjacent and just poleward of the plasmapause footprint, consistent with the SAPS flows observed in the SuperDARN data. Note that the most westward beams are more closely aligned with the SAPS flow direction and that color variations are due to both spatially varying flows and spatially varying beam directions.

Figure 4 shows electron density measurements from five different satellites during periods when each satellite was closest to the plasmapause. From top to bottom, Figure 4a shows electron density time series for

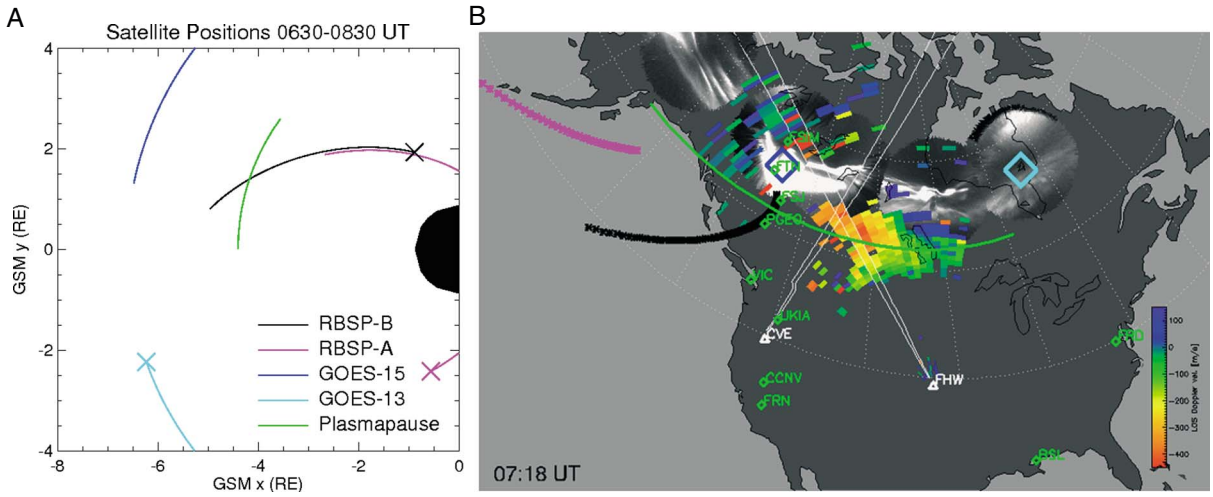


**Figure 3.** (a) GSM *xy* view of satellite trajectories from 0630 to 0830 UT. Lines with different colors indicate different satellites and the plasmapause location (green line) determined from RBSP electron density measurements. Crosses mark the start of the spacecraft trajectories at 0630 UT. (b) Map showing the geographic position of ground magnetometer stations as green diamonds and the Fort Hays West/Christmas Valley East SuperDARN radars as white triangles, the ground track of RBSP-B (black crosses), RBSP-A (pink crosses), GOES 15 (dark blue diamond), and GOES 13 (light blue diamond) from 0630 to 0830 UT, with colors consistent with Figure 3a. Two SuperDARN beams selected for analysis are marked with white lines. The plasmapause location derived from RBSP measurements is shown as a green line. Snapshots at 0718 UT of the FYKN, FSIM, FSMI, GILL, and SNKQ all-sky camera images (whiter color indicates stronger intensity) and Fort Hays West radar line of sight velocities (color scale at right) are overplotted on the map.

RBSP-B, RBSP-A, THEMIS-D, THEMIS-E, and THEMIS-A. Figure 4b shows the satellite trajectories during the periods when these measurements were taken: RBSP-B from 0630 to 0845 UT (solid black line), RBSP-A from 0745 to 1030 UT (solid pink line), THEMIS-D from 0400 to 0600 UT (dashed black line), THEMIS-E from 0630 to 0830 UT (dashed blue line), and THEMIS-A from 1115 to 1315 UT (dashed pink line). Both RBSP spacecraft are in the premidnight sector on similar orbits, while the three THEMIS spacecraft are near the dawn sector on similar orbits.

Figure 4c shows electron density measurements binned according to dipole *L* from the five spacecraft, with line styles consistent with Figure 4b; measurements from the premidnight sector are solid lines, while dawn sector measurements are dashed lines. We identify the plasmapause location as the location of sharpest density gradient. The radial density profile evolves little in the premidnight sector between the RBSP-B (0630–0845 UT) and RBSP-A (0745–1030 UT) outbound passes, as indicated by the solid black and pink lines lying nearly on top of each other. Moreover, the plasmapause location does not change between subsequent crossings at 0750 UT (RBSP-B) and 0920 UT (RBSP-A). In the dawn sector, the plasmapause moves inward from the location where THEMIS-D first measures it at 0430 UT (dashed black line) to the location where THEMIS-E observes it at 0655 UT (dashed light blue line). At 1145 UT, THEMIS-A observes it in the same location (dashed pink line), suggesting that the plasmapause remained stationary for ~5 h.

Note that THEMIS densities are inferred from spacecraft potential, and the technique to obtain the density is significantly less accurate in high-density regions (Kwon et al., 2015) depending on several factors (Laakso & Pedersen, 1998). Thus, though the plasmapause identification using THEMIS satellites is reliable, the absolute accuracy of densities at low *L* is not particularly reliable and we do not stress comparisons between satellites at low *L* values.

We estimate the plasmapause location (sharpest gradient) to be at $L \sim 4.4$ in the premidnight sector and $L \sim 4.0$ in the predawn sector during the period of interest. Figure 4b shows the plasmapause location in the premidnight sector inferred from the RBSP observations as a solid green line, while the dawn sector plasmapause from THEMIS-A and THEMIS-E is a dashed green line. Figures 3a and 3b also show the plasmapause location in the premidnight sector as a solid green line. These figures show that the two GOES spacecraft are located outside the plasmasphere and GOES 15 maps near the region of the auroral intensification at 0722 UT. In contrast, the two RBSP spacecraft are mostly inside the plasmasphere until the end of the interval, when RBSP-B crosses outside the plasmasphere.

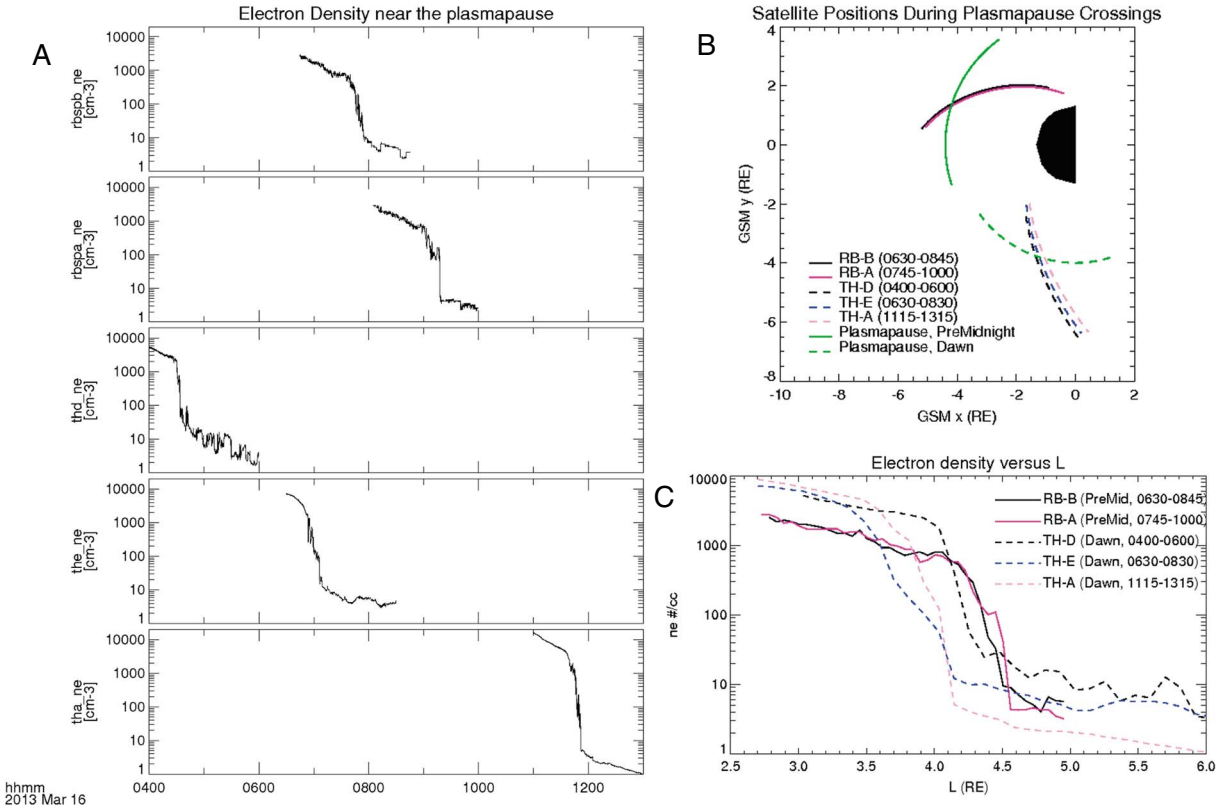


**Figure 4.** (a) Electron density measurements from five different satellite trajectories (from top to bottom): RBSP-B from 0630 to 0845 UT, RBSP-A from 0745 to 1030 UT, THEMIS-D from 0400 to 0600 UT, THEMIS-E from 0630 to 0830 UT, and THEMIS-A from 1115 to 1315 UT. (b) Orbital trajectories for each spacecraft corresponding to times shown in Figure 4a: RBSP-B (solid black line), RBSP-A (solid pink line), THEMIS-D (dashed black line), THEMIS-E (dashed blue line), and THEMIS-A (dashed pink line). The approximate plasmapause location from RBSP observations in the premidnight sector is shown as a solid green line, while the location based on THEMIS observations near dawn is shown as a dashed green line. (c) Electron density versus *L* using the same data as in Figure 4a and the same line styles as in Figure 4b.

There are many factors that control the plasmapause location in a given local time sector, including the current and previous convection electric field, refilling rates, and the previous history of the plasmasphere in other local time sectors. The observations suggest that in this particular event, the balance between all of these factors led to a stable plasmapause location between 0630 and 0830 UT. There are several lines of evidence from Figures 1 and 4 to support this claim:

1. Multiple THEMIS satellite passes demonstrate the plasmapause location evolved between 0430 and 0655 UT in the predawn sector, but it did not change substantially between 0655 UT and 1145 UT. If the primary cause of erosion and plasmapause motion is changes to the global convection electric field caused by southward IMF, one would expect changes to plasmapause location to be global in nature; if the plasmapause is stationary near dawn, it will be stationary near midnight.
2. Multiple RBSP satellite passes are consistent with (1), indicating no significant change in plasmapause location in the premidnight sector between 0750 UT and 0920 UT. The only difference between the plasmapause locations near midnight and dawn is due to the expected inward motion of cold plasma as it $\vec{E} \times \vec{B}$ drifts eastward.
3. Plasmapause motion observed by THEMIS satellites between 0430 UT and 0655 UT likely concluded before 0630 UT. Before 0600 UT, geomagnetic activity levels were decreasing and the north-south component of the IMF was close to 0 (Figure 1). Since the typical timescale for the plasmapause to move in response to IMF variations is 10–30 min (Murakami et al., 2007), plasmapause motion should have concluded by 0630 UT.
4. There is no indication of local plasmapause structures (Goldstein et al., 2005) in either the THEMIS or RBSP density profiles.

Thus, geomagnetic activity and periods of southward IMF during the 0630–0830 UT period may have led to changes in the convection electric field, but these variations did not cause significant plasmapause motion.

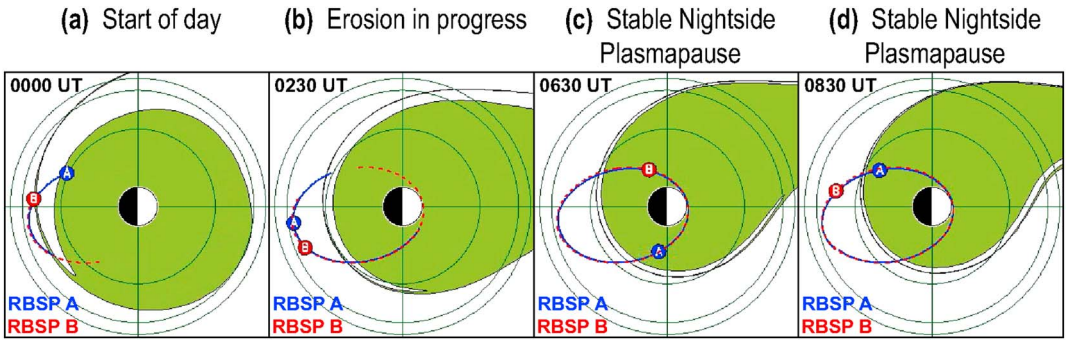


**Figure 5.** Each panel shows the plasmasphere in green, based on output from the PTP simulations. The location and orbits of the RBSP-A (blue) and RBSP-B (red) satellites are also shown. Each panel is for a different time, with the last two panels (Figures 5c and 5d) corresponding to the beginning and end of the Pi2 wave analysis interval.

For global context and as a final confirmation of this scenario, we examined Plasmapause Test Particle (PTP) simulations that have been shown to closely reproduce RBSP plasmapause observations (Goldstein et al., 2014). The time varying plasmapause location is obtained using an ensemble of cold test particles that $\vec{E} \times \vec{B}$ drift, where the convection electric field is obtained from solar wind measurements and the *Kp* index. Figure 5 shows output of the simulation at 4 times before, during, and after the Pi2 wave analysis interval. Confirming the interpretation of the satellite measurements, there is an erosion event during the first few hours of 16 March 2013 (Figures 5a and 5b), followed by relatively stable nightside plasmapause location during the wave analysis period 0630–0830 UT (Figures 5c and 5d).

### 3.3. Pi2 Wave Activity Before, During, and After Substorm

Having examined overall geomagnetic activity and plasmapause location, we next examine the spatial and temporal evolution of wave properties. Figure 6 examines the time evolution of wave activity and relationship to potential driving mechanisms. Figures 6 (first panel) and 6 (second panel) are identical to Figures 1 (first panel) and 1 (fourth panel) but for the shorter 0630–0830 UT period of interest; they are provided for context on the times of different auroral activations and solar wind driving conditions. Figures 6 (third panel) and 6 (fourth panel) are for line-of-sight velocities measured by the SuperDARN Christmas Valley East (CVE) radar at beam 2 and range gate 24 and Fort Hays West (FHW) radar at beam 9 and range gate 40. These beams and range gates correspond to the location where the two radar beams overlap in Figure 3b, in the region of intense SAPS flows. Note that while neither beam is exactly aligned with the SAPS flow direction, the FHW beam is more closely aligned with the flows while the CVE beam is nearly orthogonal to them (see Figures 2 and 3b). This is consistent with the LOS flow measurements in Figures 6 (third panel) and 6 (fourth panel). While the CVE measurement shows fairly stable 50 m/s flows throughout the interval (Figure 6 third panel), the FHW beam shows a rapidly changing background flow, starting at −100 m/s at 0700 UT and decreasing to −600 m/s by 0730 UT (Figure 6 (fourth panel). Since the FHW beam is most closely aligned with the SAPS flow direction, this trend is indicative of the increasing SAPS flows.

ULF perturbations with frequencies in the Pi2 range are also seen throughout the interval in both radars, though the signal is sometimes obscured by the time-varying background SAPS flows. Figure 6 (fifth panel) is for the north-south magnetic field (BX) measured by the FRN ground magnetometer station (daily average subtracted), while Figure 6 (sixth panel) is for the corresponding dynamic power spectrum; this station is located equatorward of the SuperDARN LOS flow measurement locations (see Figure 3b and Table 1 for location). As shown in Figure 6 (sixth panel), several intensifications in wave power are observed at 8 mHz, in some cases accompanied by intensifications at other wave frequencies. For example, during the auroral intensification at the beginning of the substorm at 0720 UT, wave power is largest at 8 mHz (dark red color), but the power spectrum has a broad peak with wave power at other higher and lower frequencies (lighter red colors above and below 8 mHz). To more clearly examine the time evolution of wave spectral features, the power spectrum at each time step is normalized to the maximum power in the 5–20 mHz frequency band in Figure 6 (seventh panel). As evidenced by the dark red band extending across nearly the entire figure, the dominant spectral feature occurs at 8 mHz. In other words, there is a peak in the power spectrum at 8 mHz for the majority of the 2 h interval. However, we note that there are several intervals where the peak frequency is lower (e.g., red line at 6 mHz at 0800 UT). These correspond to periods where the 8 mHz

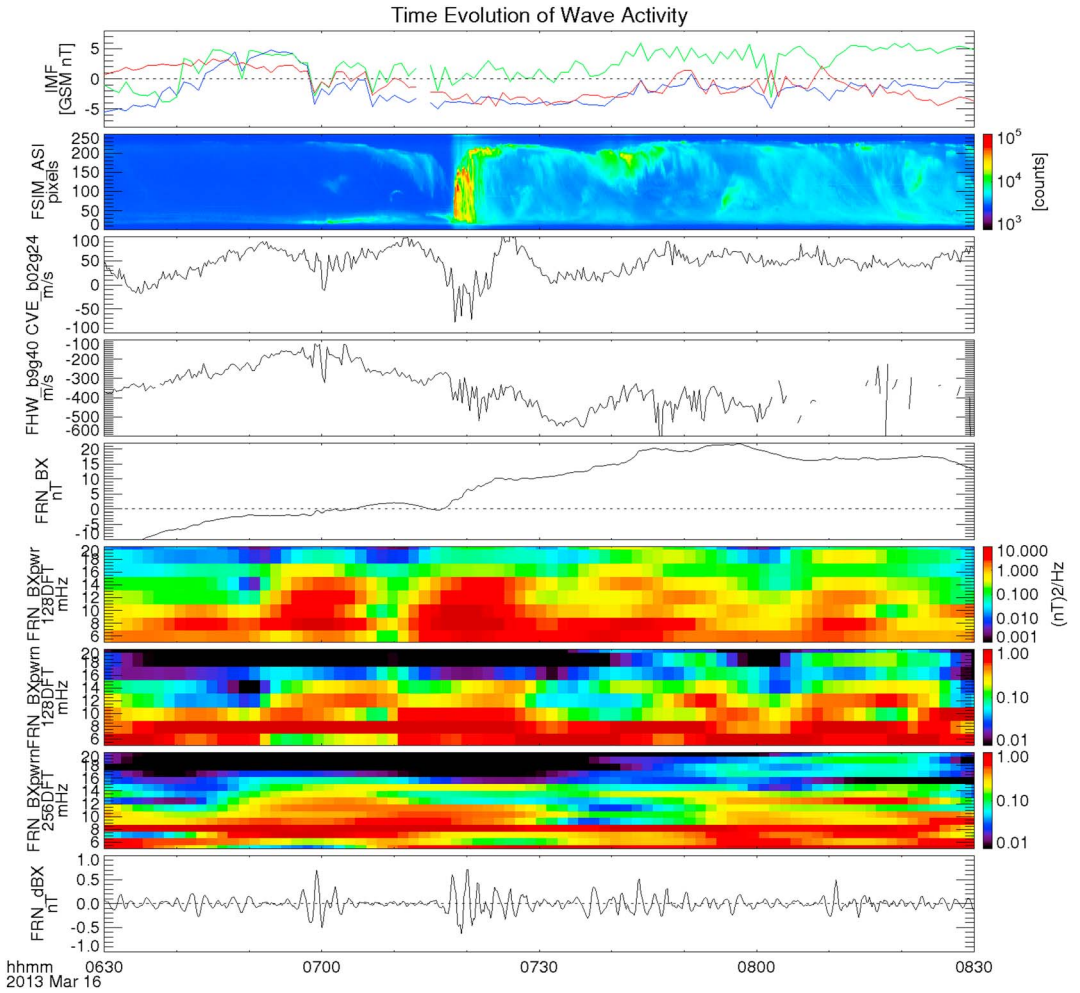


**Figure 6.** From top to bottom, (first panel) OMNIWeb IMF in GSM coordinates (same as Figure 1), (second panel) keogram from Fort Simpson all sky imager (same as Figure 1), (third panel) line-of-sight velocity measured by the SuperDARN Christmas Valley East radar at beam 2 and gate 24, (fourth panel) the same for the Fort Hays West radar at beam 9 and gate 40 (note that these beams and gates correspond to the location where the two radar beams overlap in Figure 3), (fifth panel) north-south component of magnetic field, BX, measured by FRN ground station, (sixth panel) dynamic power spectrum for BX at FRN, (seventh panel) normalized BX power spectrum at FRN, where the power spectrum at each time step is normalized to the maximum power in the 5-20 mHz frequency band, (eighth panel) the same as 7, but using a DFT window that is twice as long (256 compared to 128 point, or 47.0 minutes compared to 23.5 minutes), (ninth panel) high-pass filtered BX at FRN with 5 mHz cutoff.

signal weakens relative to other wave activity and may not be detectable (Figure 6, sixth panel). We return to this point in section 4.

To better resolve the frequency of these waves and assess the stability of the 8 mHz signal during the period of interest, we doubled the DFT window length (256 point, 47 min) in Figure 6 (eighth panel). Recall from section 2 that this increases the frequency resolution by a factor of 2. The results are similar to Figure 6 (seventh panel) with a more narrow red line that extends across the figure. Based on these results and the width of the DFT frequency bins, we conclude that the dominant spectral feature observed at FRN occurs at a frequency of $8.2 \pm 0.53$ mHz during most of the 2 h interval. In a future study, more sophisticated signal processing tools could be used to better resolve the frequency. In the present study, we can at least say the frequency was stable in the range of $8.2 \pm 0.53$ mHz through multiple intensification during the 2 h interval (note the 47 min DFT windows near the beginning of the 2 h interval do not overlap with those at the end).

Finally, Figure 6 (ninth panel) shows high-pass filtered BX time series at FRN to more directly compare with SuperDARN LOS flow time series in Figures 6 (third panel) and 6 (fourth panel). Intensifications in 8 mHz wave activity occur at 0700 and 0720 UT in all three time series.

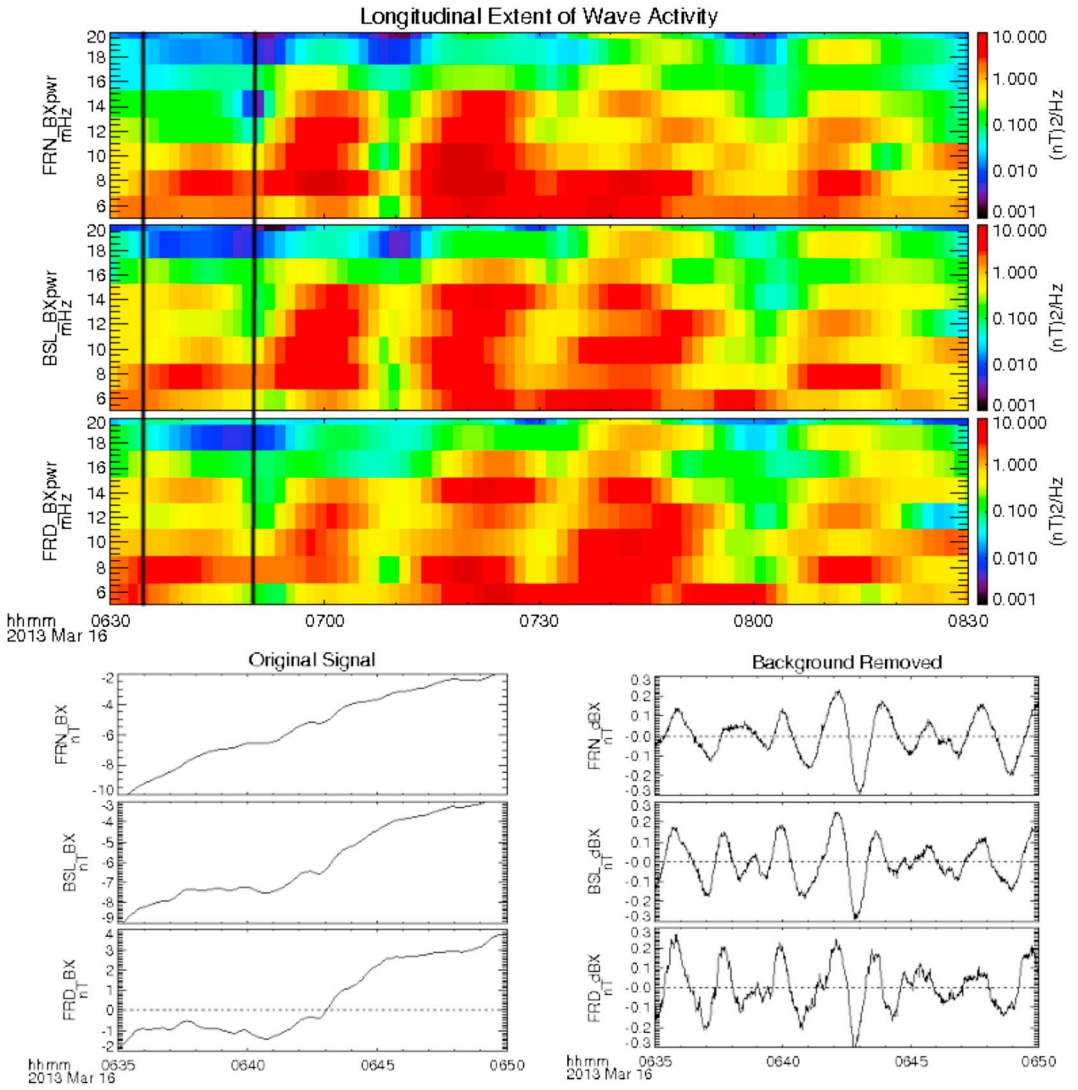


**Figure 7.** (top) From top to bottom, BX dynamic power spectrum at the FRN, BSL, and FRD ground magnetometers. Solid lines mark the time interval analyzed in the bottom of the figure. (bottom left column) From top to bottom, the original (apart from daily average subtraction) north-south magnetic field measurement at the FRN, BSL, and FRD stations between 0635 and 0650 UT. Though small compared to background trends, there are noticeable perturbations with roughly 2 minute periodicity. (bottom right column) The same as Figure 7 (bottom left column), but with background trends removed using a high-pass filter with 5 mHz cutoff. Though separated by several degrees in magnetic latitude and longitude, all three stations observe similar perturbations with very small time lags.

More information about the global extent of wave activity observed at low latitudes is shown in Figure 7. The top three panels are for the BX dynamic power spectrum at the FRN (same as Figure 6, sixth panel), BSL, and FRD stations, respectively. These stations extend across roughly 55° magnetic longitude (roughly 3.5 h MLT) and 5° magnetic latitude. Despite their spatial separation, they observe similar temporal evolution of the wave power spectrum, though FRN tends to observe slightly larger wave powers likely due to its proximity to the most intense auroral intensification (Figure 3b), consistent with previous studies of Pi2 waves (Nosé et al., 2008).

The bottom panels of Figure 7 illustrate the similarities in wave activity at these three stations by examining the relatively quiet 0635–0650 UT interval. Figure 7 (bottom left column) shows the original (apart from daily average subtraction) north-south magnetic field measurement at FRN, BSL, and FRD. Though the background trend is larger than the perturbation amplitudes, perturbations with similar periods can still be seen at all stations. Figure 7 (bottom right column) further illustrates the similarities in wave activity by showing the signal with background trend removed using a high-pass filter with 5 mHz cutoff. During this 15 min interval, 8 mHz

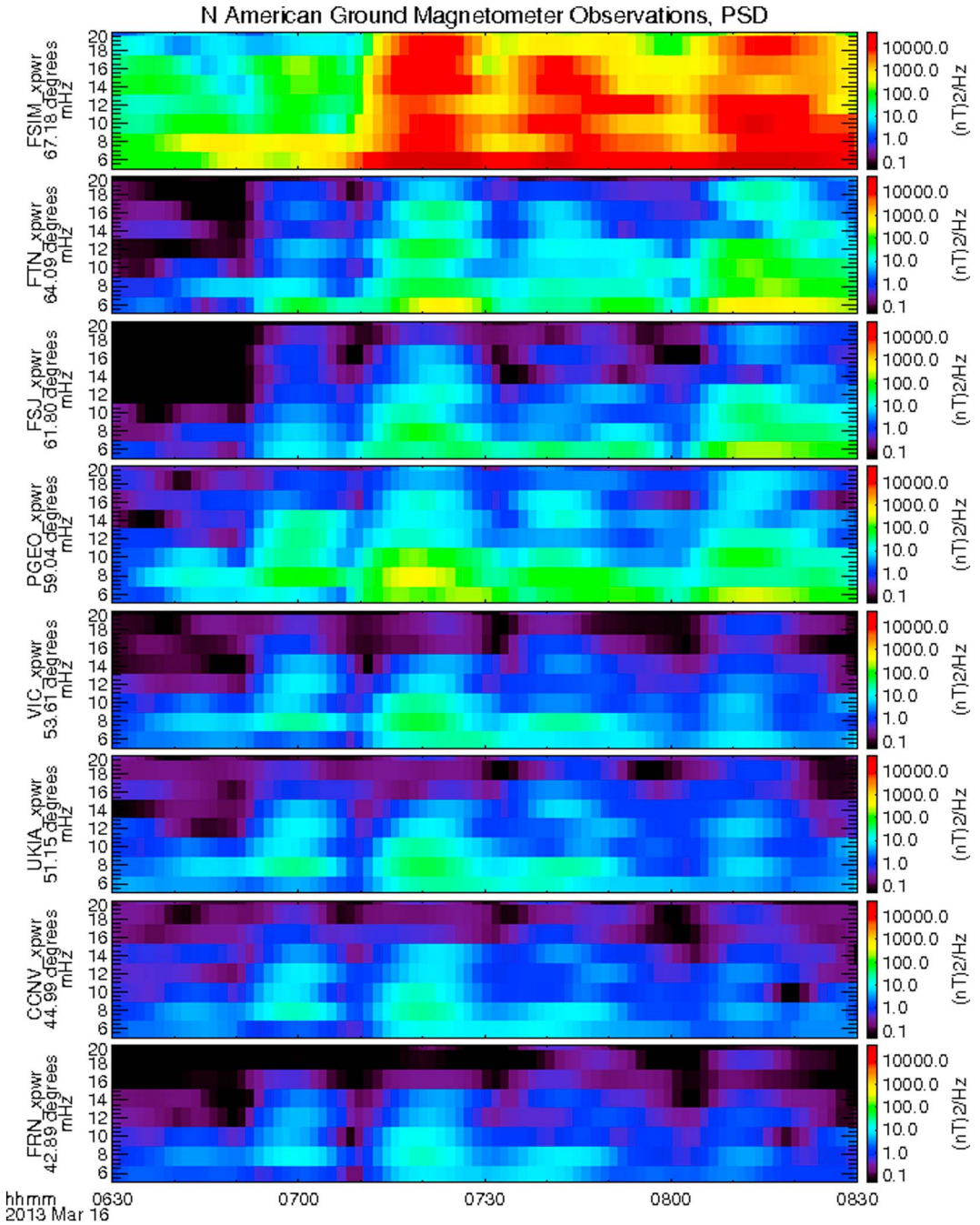


**Figure 8.** Dynamic power spectra for BX measured at several ground magnetometer stations, all on the same scale and ordered according to magnetic latitude, with highest latitude at the top: FSIM, FTN, FSJ, PGEO, VIC, UKIA, CCNV, and FRN. The geomagnetic latitude for each station is indicated on the *x* axis label.

fluctuations with similar amplitude are seen at all stations with almost no time lag. Given the roughly 3.5 h MLT and 5° latitude separation of these stations, this similarity suggests that the waves are globally coherent with negligible frequency change versus latitude or longitude. Note that the perturbation amplitudes are roughly 10 times larger than the sensitivities of the USGS magnetometers (0.01 to 0.02 nT, Worthington et al., 2009).

We next examine how wave properties vary with magnetic latitude. Figure 8 shows dynamic power spectra from ground magnetometer stations along a similar meridian in western Canada and the United States (Figure 3b). Stations are ordered from highest latitude on top to lowest latitude at the bottom: FSIM, FTN, FSJ, PGEO, VIC, UKIA, CCNV, and FRN. Recall from Figure 3b that PGEO and FSJ are closest to the plasmapause and

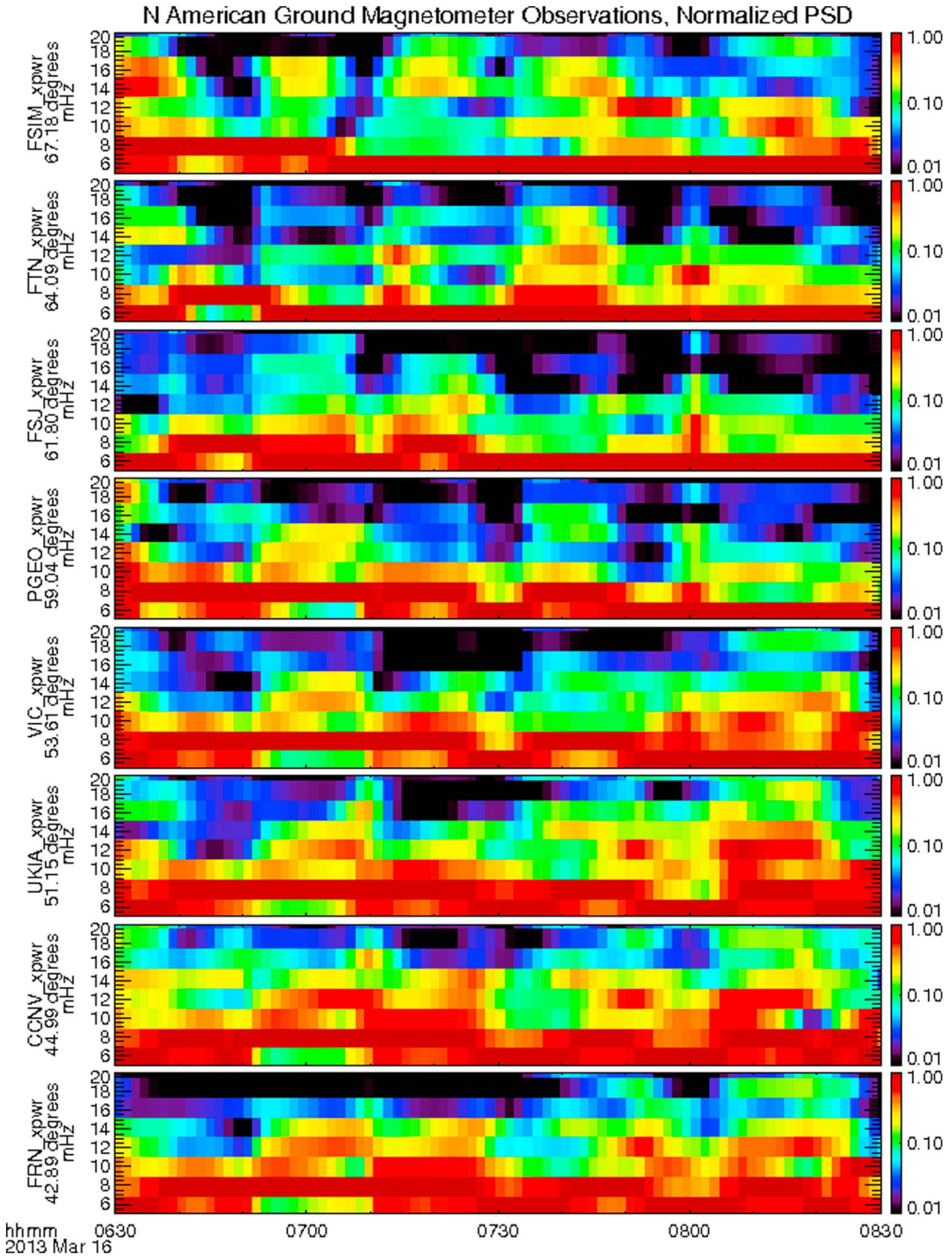


**Figure 9.** The same as in Figure 8 but for normalized dynamic power spectra to emphasize spectral features. At each time step, all power values from Figure 8 are all divided by the maximum power in the frequency range from 5 to 20 mHz. The geomagnetic latitude for each station is indicated on the *x* axis label.

that FSJ, FTN, and FSIM all map to locations outside the plasmapause. All dynamic power spectra are plotted using the same scale. The lowest latitude FRN, CCNV, UKIA, and VIC stations tend to observe the smallest wave amplitudes (blue-green colors at most frequencies/times), PGEO, FSJ, and FTN observe intermediate amplitudes (green colors at most frequencies and times), while FSIM observes significantly larger wave amplitudes (yellow and red colors at most frequencies/times). The 8 mHz signal seen in earlier figures appears most

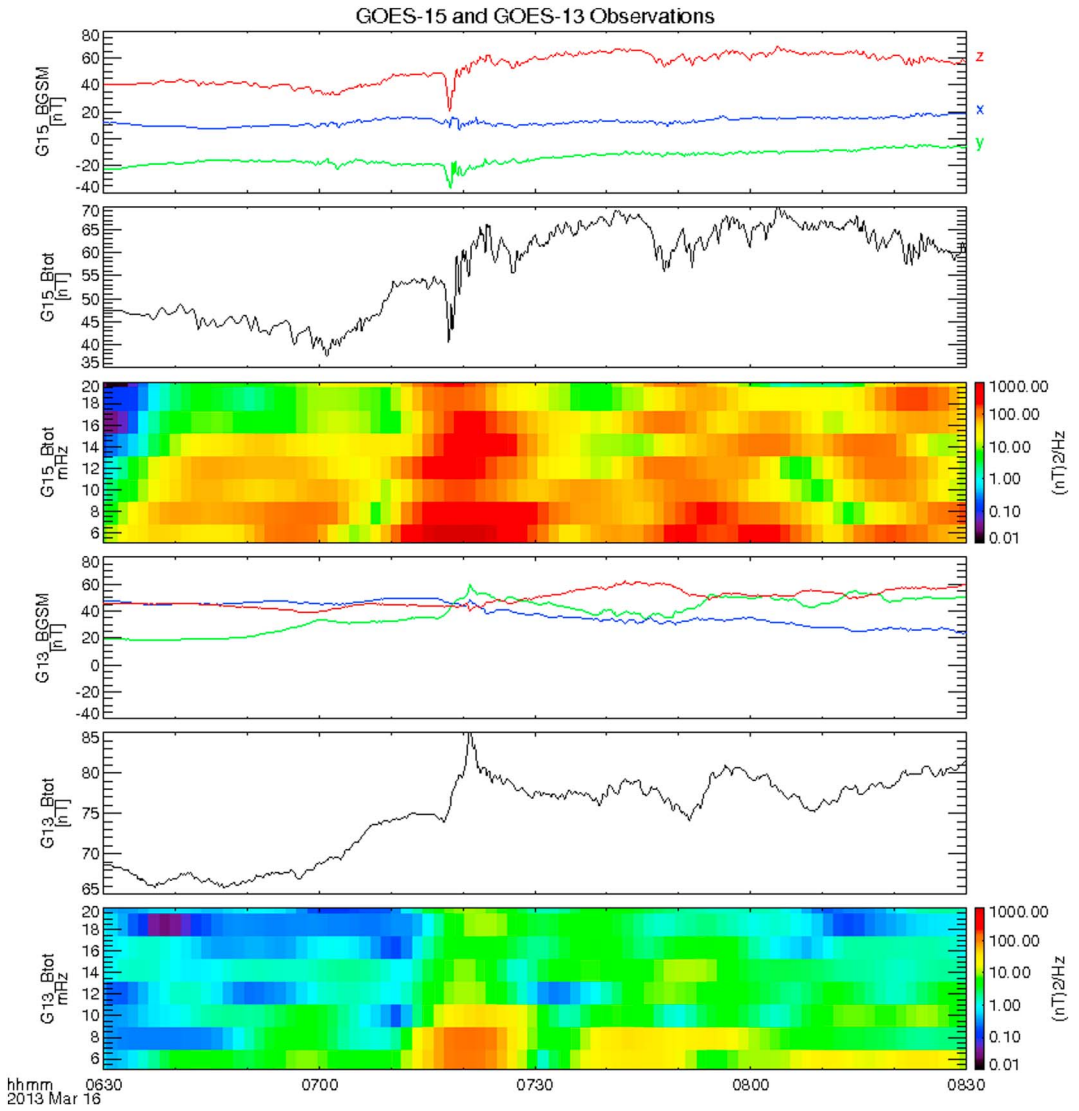


**Figure 10.** From top to bottom, (first panel) magnetic field measurement from GOES 15 in GSM coordinates, (second panel) total magnetic field measured by GOES 15, (third panel) dynamic power spectrum of GOES 15 total magnetic field perturbations, (fourth–sixth panels) the same as Figures 10 (first panel)–10 (third panel), but for GOES 13.

clearly at the lower latitude stations, though all stations observe it during periods when other wave activity with more broadband frequency spectra is not present, such as the 0635–0650 UT interval.

Figure 9 is the same as Figure 8, except that the power spectra have been normalized in the same manner as in Figure 6 (seventh panel). The 8 mHz signal dominates the normalized spectra throughout the 2 h interval for stations at latitudes below 60°, as indicated by the solid red band across the bottom five panels at 8 mHz. At higher latitudes, the 8 mHz signal is also present for at least part of the interval, but as discussed above it is less often the dominant spectral feature. For example, there are intervals where the peak frequency is lower (i.e., red line at 6 mHz for most of the interval in the top three panels). The disappearance of the red band at 8 mHz does not necessarily indicate that the original 8 mHz wave activity has damped out. Instead, these monochromatic waves may be obscured by larger amplitude wave activity with a more broadband frequency spectrum that overlaps 8 mHz. We return to this point in section 4.

We next turn our attention to in situ GOES 15 and GOES 13 satellite measurements of wave activity outside the plasmapause. Figures 10 (first panel) and 10 (fourth panel) are for the three components of the magnetic field in GSM coordinates measured by GOES 15 and GOES 13, respectively. When compared to GOES 13,

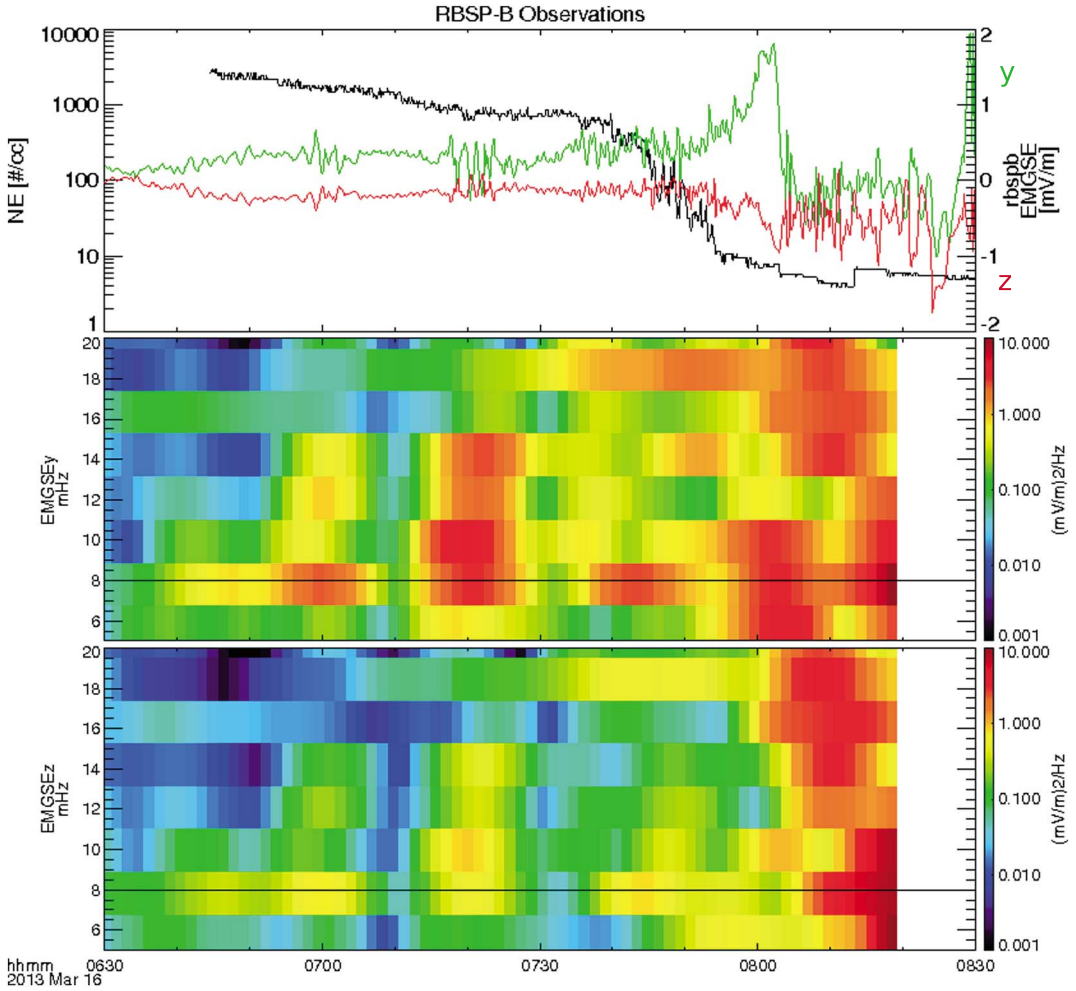


**Figure 11.** From top to bottom, (top) RBSP-B electron density (black) and *y* (green) and *z* (red) components of the electric field in MGSE coordinates, (middle) dynamic power spectrum for the electric field MGSE *y* component, (bottom) the same as Figure 11 (middle) but for the *z* component.

the GOES 15 magnetic field experiences a much larger deflection near 0718 UT, accompanied by larger fluctuations. This is roughly the time the particle injection was observed by GOES 15 (Figure 1) and when the large auroral arc was observed near the footpoint of GOES 15 (Figures 1, fourth panel and 3b). These observations indicate the largest disturbances associated with the substorm are in the premidnight sector near the GOES 15 satellite location. This is also reflected in Figures 10 (second panel) and 10 (fifth panel), showing total magnetic field measured by GOES 15 and GOES 13, respectively. Noting the *y* axis scale difference, GOES 15 observes generally larger total magnetic field perturbations than GOES 13.

Figures 10 (third panel) and 10 (sixth panel) are for the dynamic power spectrum of the total magnetic field observed by GOES 15 and GOES 13, respectively. GOES 15 observes systematically larger amplitude fluctuations at most frequencies and times. Given the spacecraft positions (Figure 3a), this suggests that wave activity outside the plasmasphere is more intense premidnight when compared to postmidnight. Generally, compressional wave activity observed by both GOES probes has a broader frequency spectrum than wave activity observed on the ground, with the frequency range of enhanced wave power including, but not necessarily peaking at, 8 mHz.

Finally, we examine in situ wave activity inside and immediately outside the plasmasphere using RBSP-B observations in Figure 11. During the period of interest, the RBSP-B satellite was moving away from the Earth in the premidnight sector, at a similar local time to the GOES 15 satellite (Figure 3a). Figure 11 (top) shows electron density measured by RBSP-B as a black line, indicating that it crossed out of the high-density plasmasphere at roughly 0750 UT. This panel also shows the unfiltered *y* (green) and *z* (red) Modified Geocentric

Solar Ecliptic (MGSE) components of the electric field. In MGSE coordinates, $x_{MGSE}$ points along the spacecraft spin axis and is usually close to the $x_{GSE}$ direction (Earth-Sun line), $y_{MGSE}$ points along $z_{GSE} \cdot x_{MGSE}$ (in the spin plane and ecliptic plane, close to the $y_{GSE}$/duskward direction), and $z_{MGSE}$ completes the right-handed orthogonal set, in the spin plane and close to the normal to the ecliptic plane. Figure 11 (middle) shows the dynamic power spectrum for the MGSE *y* component of the electric field, while Figure 11 (bottom) is for the *z* component. Both panels indicate several periods with discrete frequency 8 mHz wave activity (e.g., 0640–0700 UT) and periods with intensification of more broadband frequency wave activity that includes 8 mHz but peaks at other frequencies (e.g., 0720 UT). Upon crossing the plasmapause, larger-amplitude fluctuations are seen with a broader frequency spectrum, consistent with GOES observations (Figure 10).

We also examined RBSP total magnetic field perturbations (not shown), finding small amplitude perturbations and signals with 8 mHz frequency most clear during the early part of the interval when RBSP is at lower *L*. If the 8 mHz signal is associated with a PVR, the fact that it is most clear at low *L* may be related to the presence of a node in magnetic field perturbations at spatial locations near the plasmapause, as reported in previous PVR studies (Takahashi et al., 2010). Magnetic field perturbations in different components also had small amplitudes and were dominated by the presence of an artificial 5 min nutation signal (result of removing star tracker from spacecraft) during part of the interval.

## 4. Discussion

In the previous section, we presented several observations of nightside Pi2 wave properties during an extended period with stable plasmapause location and variable geomagnetic wave activity. To summarize, the following are observations from 0630–0830 UT on 16 March 2013:

1. *Solar wind and geomagnetic activity*: Southward IMF and several sharp decreases in *AL* for much of the early part of the day, then relatively quiet conditions in the nightside magnetosphere at the beginning of the interval of interest until roughly 0716 UT when a substorm occurs and SAPS flows as large as 800 m/s develop.
2. *Plasmapause location*: Multiple satellite passes suggest the plasmapause location does not change between 0630 and 0830 UT. The radial density profile also changes little in the premidnight sector between the RBSP-B (0630–0845 UT) and RBSP-A (0745–1030 UT) outbound passes. PTP simulations based on solar wind observations and the *Kp* index confirm this scenario.
3. *Pi2 wave activity, latitudinal extent*: 8 mHz signal is observed clearly by the RBSP-B satellite when inside the plasmasphere. It is also observed by ground-based magnetometers at magnetic latitudes ranging from 41 to 67° ($L = 1.8$ to 6.6), mapping to locations both inside and outside the plasmapause. Outside the plasmasphere, the 8 mHz signal may be obscured by larger-amplitude wave activity with a broadband frequency spectrum; for example, both RBSP-B and GOES satellites observe Pi2 wave activity with a broader frequency spectrum outside the plasmasphere, and the highest latitude FSIM ground station observes similar features during later parts of the 0630–0830 UT interval.
4. *Pi2 wave activity, longitudinal extent*: Low-latitude stations separated by 3.5 h MLT observe very similar 8 mHz wave forms with negligible time lags.
5. *Pi2 wave activity, time evolution*: 8 mHz signal is observed throughout the 0630–0830 UT interval before, during, and after (1) the substorm, (2) other auroral intensifications, (3) the development of SAPS flows, and (4) variations in the IMF. Wave amplitudes vary in time at all locations and are strongest at the beginning of the substorm.

The 8 mHz wave observations are consistent with models of radially standing MHD fast mode waves such as PVR: same frequency observed across a wide range of latitude/longitude, frequency does not change through multiple intensifications as long as the radial density/Alfvén speed profile does not change, very small time lags between signals observed at stations separated by 3.5 h MLT suggest globally coherent wave activity with very small (∼0) azimuthal wave number, strong in situ electric field perturbations in conjunction with weak total magnetic field perturbations suggest nodal structure (Keiling & Takahashi, 2011; Li et al., 1998; Nosé et al., 2008). Phase differences between in situ electric field and ground-based observations were also consistent with PVR during periods when the RBSP-B electric field MGSE measurement was roughly aligned with the east-west direction, and in situ and ground-based measurements had a high degree of coherence, consistent with previous studies (Takahashi et al., 2009); for brevity sake we have not shown these observations. We shall refer to these waves as a PVR rather than another standing fast mode wave (e.g., plasmaspheric cavity mode)

primarily due to observations in Figures 8 and 9 indicating the presence of monochromatic wave activity at latitudes mapping outside the plasmapause, particularly before 0700 UT. However, the distinction between PVR and other standing fast mode waves is not important to the conclusions of this study, since all such waves are sensitive to the radial density profile and plasmapause location.

Taken as a whole, the 8 mHz wave observations summarized above are also inconsistent with other Pi2 wave models. For example, Alfvén waves standing along the background magnetic field could not produce the same discrete frequency wave activity at different latitudes with no observable time lags (Figures 7 and 8). BBFs could not continuously generate the same frequency wave activity throughout the entire 2 h interval, during both active and quiet conditions. However, with regard to the more broadband frequency wave activity observed at higher latitudes, BBFs/plasma sheet flow bursts are a plausible generation mechanism (e.g., Nishimura et al., 2012; Ream et al., 2015). Finally, the PGEO ground station close to the plasmapause (Figure 3b) observes locally enhanced power at 8 mHz when compared to adjacent stations, suggestive of a plasmapause surface wave. However, we can discard the plasmapause surface wave explanation in this study based on the small phase differences between 8 mHz signals measured at longitudinally separated stations (Figure 7), since such waves are expected to have large azimuthal wave numbers (Chen & Hasegawa, 1974). Instead, this feature may relate to (1) radial PVR structure or field line resonances associated with radial density gradients at the plasmapause, (2) latitudinal ionospheric conductivity variations, or (3) a combination of (1) and (2) (e.g., Keiling & Takahashi, 2011; Lysak et al., 2015; Shi et al., 2017; Takahashi et al., 2003). Identifying the source(s) of features such as these requires detailed comparisons with numerical simulations and is thus an important topic for future work, and this study provides important constraints for such simulations, including the radial density profile.

The stable radial plasma density profile and plasmapause location during variable geomagnetic activity is a unique feature of this event. Since PVR properties depend strongly on these factors, this event presents an opportunity to examine how other factors, such as time variable external driving conditions (IMF, multiple BBFs, and substorm) and ionospheric boundary conditions (e.g., SAPS flows and accompanying conductivity variations) affect PVR properties. In this event, we find that these other factors do not affect the PVR frequency, as the 8 mHz signal is stable throughout the interval. By "stable" we mean that the frequency of wave activity does not change from one wave intensification to the next, within the accuracy of the DFT analysis. More specifically, the 256-point DFT analysis shown in Figure 6 (eighth panel) indicates a persistent spectral feature with a frequency of $8.2 \pm 0.53$ mHz. The DFT window is 47 min long while the interval is 2 h; thus, the frequency of this feature obtained from DFT windows at the beginning of the interval is the same as the frequency at the end of the interval, to within the frequency uncertainty of the DFT analysis (see section 2 for more discussion of uncertainty). There are locations and times when the 8.2 mHz signal is either not present or not detectable due to low amplitudes or the presence of other waves, but subsequent intensifications indicate a natural response frequency of the plasmasphere that does not change.

However, external driving conditions and/or ionospheric variability must play a role in the temporal and spatial variability of the PVR amplitude. These factors also affect other types of ULF wave activity that are important to the generation and detection of PVR. For example, waves with broadband frequency spectrum and large amplitudes were observed outside the plasmasphere in this study. These waves may be an energy source for the PVR while also obscuring the PVR from detection. In particular, the FSIM station observes significantly larger amplitude perturbations than other stations, and these perturbations tend to have a broadband frequency spectrum (Figure 8, first panel). There are a few explanations for these features, not mutually exclusive: (1) radial PVR structure determined by the radial density profile, (2) high-latitude Pi2 waves that may act as an energy source of the PVR, such as flow bursts and related Alfvén waves occurring outside the plasmapause (see Keiling & Takahashi 2011 for additional high-latitude Pi2 models), (3) latitudinal variations in ionospheric conductivity that affect the amplitude of ground magnetic perturbations and the closure of magnetospheric currents. Items (1)–(3) could independently, or together, result in the differences seen at FSIM, and it is possible for a both PVR and other types of Pi2 waves to be observed simultaneously at FSIM's high-latitude location. Numerical simulations are beginning to resolve this type of ambiguity (e.g., Lysak et al., 2015), but fully explaining the features seen at FSIM in the context of (1)–(3) is outside the scope of the present study.

Finally, we note that if we had only considered observations during a narrow time range near substorm onset or a limited spatial range (e.g., near SAPS flows or plasmapause location), we may well have associated the 8 mHz wave activity with BBFs, plasmapause surface waves, or another Pi2 model. This demonstrates the need

**Acknowledgments**
M. D. Hartinger was supported by NSF grant AGS-1342968 and NASA grant NNX17AD35G. S. Zou was supported by NSF grant AGS-1342968. K. Takahashi was supported by NASA grant NNX15AI95G. X. Shi was supported by NSF grant AGS-1341918. RBSP electron density data used in this paper are available from http://emfsis.physics.uiowa.edu. The research at University of Iowa was supported by JHU/APL contract 921647 under NASA prime contract NAS5-01072. The work by the RBSP EFW team was conducted under JHU/APL contract 922613 (RBSP-EFW). We acknowledge the use of SuperDARN Data publicly available at http://vt.superdarn.org/.SuperDARN is a collection of radars funded by national scientific funding agencies of Australia, Canada, China, France, Italy, Japan, Norway, South Africa, United Kingdom, and the United States. All ground magnetometer data are publicly available at http://themis.ssl.berkeley.edu/data/themis/thg/l2/mag/. We acknowledge the use of data collected at magnetic observatories operated by the U.S. Geological Survey (USGS, geomag.usgs.gov). We thank I. R. Mann, D. K. Milling and the rest of the CARISMA team for data. CARISMA is operated by the University of Alberta, funded by the Canadian Space Agency (http://www.carisma.ca/). We acknowledge NASA contract NAS5-02099 and V. Angelopoulos for use of data from the THEMIS Mission. Specifically, S. Mende and C. T. Russell for use of the GMAG data and NSF for support through grant AGS-1004814; the Canadian Magnetic Observatory Network (CANMON) maintained and operated by the Geological Survey of Canada (http://www.geomag.nrcan.gc.ca); Kanji Hayashi, University of Tokyo for use of magnetometer data from the Solar-Terrestrial Energy Program Polar Network (http://step-p.dyndns.org/~khay/). We thank the NASA Space Science Data facility for use of solar wind data and geomagnetic activity indices. We thank Haje Korth for providing the Geopack interface as part of the SPEDAS software package and Kolya Tsyganenko for creating the Geopack library and external field models. Magnetic field input parameters (derived from data on OMNIWeb) were provided by Richard Denton and Zhengui Qin. Data and the SPEDAS software package used for this study can be obtained from the THEMIS website (themis.ssl.berkeley.edu/index.shtml, software version r22843). We thank Aaron Breneman, Michael Ruohoniemi, and Scott Bounds for useful discussions and data interpretation.

for globally distributed observations and extended analysis periods when associating Pi2 wave observations with different wave sources, as noted by Keiling and Takahashi (2011).

## 5. Summary

The frequencies and amplitudes of Pi2 waves such as PVR are strongly affected by the plasmapause location. The present study extends previous work relating Pi2 wave activity to plasmapause location (e.g., Ghamry et al., 2015; Shi et al., 2017; Takahashi et al., 2003, 2005) by examining wave activity during an extended interval with stable plasmapause location and variable geomagnetic activity. The following items summarize our key findings:

1. Multiple-satellite passes and PTP simulations indicate that the plasmapause location is stable for at least 2 h over a wide range of MLT. This stability allows us to examine how other factors affect Pi2 wave properties.
2. Both in situ and ground-based measurements indicate multiple intensifications of a PVR through a period of variable geomagnetic activity. Other wave activity with a more broadband frequency spectrum also occurs, primarily outside the plasmapause.
3. PVR wave amplitudes vary spatially and temporally while frequency remains stable at $8.2 \pm 0.53$ mHz, based on low-latitude ground magnetometer observations. The frequency is stable throughout multiple wave intensifications that occur before, during, and after (1) a substorm, (2) multiple auroral intensifications, (3) the development of SAPS flows and associated ionospheric conductivity variations, and (4) variations in the IMF. The stable frequency is consistent with PVR model predictions—and other standing fast mode wave model predictions—for a stable plasmapause location.

Stable plasmapause locations are necessary for stable PVR frequencies. In this study, we found that a stationary plasmapause before, during, and after a substorm was likely caused by a prolonged period of southward IMF preceding the interval of interest, during which the plasmapause location changed and erosion occurred. We speculate that conditions similar to those found in the present study—that is, periods with substorms or other Pi2 energy sources occurring after a significant erosion event—may be favorable for stable PVR frequencies due to stable density conditions.

To better understand the spatial and temporal variability of Pi2 wave activity during geomagnetically active periods, more work is needed to examine how wave properties vary during periods with relatively stable plasmapause locations such as the one in the present study. In particular, observational comparisons with global numerical simulations (e.g., Claudepierre et al., 2016; Lysak et al., 2015; Ream et al., 2015) during periods with stable plasmapause location are needed to better characterize the role of other factors (e.g., spatially varying ionospheric conductivity and time-varying driving conditions) besides the radial density profile in determining wave properties and understanding why PVR are excited during some periods but not others (e.g., Nishimura et al., 2012; Osaki et al., 1998).

## References

Anderson, P. C., Hanson, W. B., Heelis, R. A., Craven, J. D., Baker, D. N., & Frank, L. A. (1993). A proposed production model of rapid subauroral ion drifts and their relationship to substorm evolution. *Journal of Geophysical Research*, *98*, 6069–6078.

Archer, M. O., Hartinger, M. D., Walsh, B. M., & Plaschke, F. (2015). Frequency variability of standing Alfvén waves excited by fast mode resonances in the outer magnetosphere. *Geophysical Research Letters*, *42*, 10,150–10,159, https://doi.org/10.1002/2015GL066683

Archer, M. O., Hartinger, M. D., Walsh, B. M., & Angelopoulos, V. (2017). Magnetospheric and solar wind dependences of coupled fast-mode resonances outside the plasmasphere. *Journal of Geophysical Research: Space Physics*, *122*, 212–226. https://doi.org/10.1002/2016JA023428

Claudepierre, S. G., Toffoletto, F. R., & Wiltberger, M. (2016). Global MHD modeling of resonant ULF waves: Simulations with and without a plasmasphere. *Journal of Geophysical Research: Space Physics*, *121*, 227–244. https://doi.org/10.1002/2015JA022048

Chen, L., & Hasegawa, A. (1974). A theory of long-period magnetic pulsations: 2. Impulse excitation of surface eigenmode. *Journal of Geophysical Research*, *79*, 1033–1037.

Foster, J. C., & Vo, H. B. (2002). Average characteristics and activity dependence of the subauroral polarization stream. *Journal of Geophysical Research*, *107*(A12), 1475. https://doi.org/10.1029/2002JA009409

Fujita, S., & Tanaka, T. (2013). Possible generation mechanisms of the Pi2 pulsations estimated from a global MHD simulation. *Earth, Planets and Space*, *65*, 7.

Ghamry, E., Kim, K.-H., Kwon, H.-J., Lee, D.-H., Park, J.-S., Choi, J., … Huang, J. (2015). Simultaneous Pi2 observations by the Van Allen Probes inside and outside the plasmasphere. *Journal of Geophysical Research: Space Physics*, *120*, 4567–4575. https://doi.org/10.1002/2015JA021095

Goldstein, J., Burch, J. L., Sandel, B. R., Mende, S. B., C:Son Brandt, P., & Hairston, M. R. (2005). Coupled response of the inner magnetosphere and ionosphere on 17 April 2002. *Journal of Geophysical Research*, *110*, A03205. https://doi.org/10.1029/2004JA010712

Goldstein, J., De Pascuale, S., Kletzing, C., Kurth, W., Genestreti, K. J., Skoug, R. M., … Spence, H. (2014). Simulation of Van Allen Probes plasmapause encounters. *Journal of Geophysical Research: Space Physics*, *119*, 7464–7484. https://doi.org/10.1002/2014JA020252

Hartinger, M., Moldwin, M. B., Angelopoulos, V., Takahashi, K., Singer, H. J., Anderson, R. R., … Wygant, J. R. (2010). Pc5 wave power in the quiet-time plasmasphere and trough: CRRES observations. *Geophysical Research Letters*, *37*, L07107. https://doi.org/10.1029/2010GL042475

Jacobs, J. A., Kato, Y., Matsushita, S., & Troitskaya, V. A. (1964). Classification of geomagnetic micropulsations. *Journal of Geophysical Research*, *69*, 180–181.

Keiling, A., & Takahashi, K. (2011). Review of Pi2 models. *Space Science Reviews*, *161*, 63–148.

Kepko, L., Kivelson, M. G., & Yumoto, K. (2001). Flow bursts, braking, and Pi2 pulsations. *Journal of Geophysical Research*, *106*, 1903–1916.

Kivelson, M. G., Etcheto, J., & Trotignon, J. G. (1984). Global compressional oscillations of the terrestrial magnetosphere - The evidence and a model. *Journal of Geophysical Research*, *89*, 9851–9856.

Kletzing, C. A., Kurth, W. S., Acuna, M., MacDowall, R. J., Torbert, R. B., Averkamp, T., … Tyler, J. (2013). The Electric and Magnetic Field Instrument Suite and Integrated Science (EMFISIS) on RBSP. *Space Science Reviews*, *179*, 127–181.

Kwon, H.-J., Kim, K.-H., Jee, G., Park, J.-S., Jin, H., & Nishimura, Y. (2015). Plasmapause location under quiet geomagnetic conditions ($Kp \leq 1$): THEMIS observations. *Geophysical Research Letters*, *42*, 7303–7310. https://doi.org/10.1002/2015GL066090

Kurth, W. S., De Pascuale, S., Faden, J. B., Kletzing, C. A., Hospodarsky, G. B., Thaller, S., & Wygant, J. R. (2015). Electron densities inferred from plasma wave spectra obtained by the Waves instrument on Van Allen Probes. *Journal of Geophysical Research: Space Physics*, *120*, 904–914. https://doi.org/10.1002/2014JA020857

Laakso, H., & Pedersen, A. (1998). Ambient electron density derived from differential potential measurements. In Pfaff, R. F., Borovsky, J. E., & Young, D. T. (Eds.), *Measurement techniques in space plasmas: Particles* (Vol. 102, 49 pp.). Washington, DC: Published by the American Geophysical Union as part of the Geophysical Monograph Series.

Lee, D. H., & Kim, K. (1999). Compressional MHD waves in the magnetosphere: A new approach. *Journal of Geophysical Research*, *104*, 12,379–12,386.

Li, Y., Fraser, B. J., Menk, F. W., Webster, D. J., & Yumoto, K. (1998). Properties and sources of low and very low latitude Pi2 pulsations. *Journal of Geophysical Research*, *103*, 2343–2358.

Luo, H., Chen, G., Du, A., Angelopoulos, V., Xu, W., Zhao, X., & Wang, Y. (2011). THEMIS multipoint observations of Pi2 pulsations inside and outside the plasmasphere. *Journal of Geophysical Research*, *116*, A12206. https://doi.org/10.1029/2011JA016746

Love, J. J., & Finn, C. A. (2011). The USGS geomagnetism program and its role in space weather monitoring. *Space Weather*, *9*, S07001. https://doi.org/10.1029/2011SW000684

Lysak, R. L., Song, Y., Sciffer, M. D., & Waters, C. L. (2015). Propagation of Pi2 pulsations in a dipole model of the magnetosphere. *Journal of Geophysical Research: Space Physics*, *120*, 355–367. https://doi.org/10.1002/2014JA020625

Mann, I. R., Milling, D. K., Rae, I. J., Ozeke, L. G., Kale, A., Kale, Z. C., … Singer, H. J. (2008). The upgraded CARISMA magnetometer array in the THEMIS era. *Space Science Reviews*, *141*, 413–451.

Mauk, B. H. N. J., Kanekal, S. G., Kessel, R. L., Sibeck, D. G., & Ukhorskiy, A. (2012). Science objectives and rationale for the Radiation Belt Storm Probes Mission. *Space Science Reviews*, *179*, 3–27. https://doi.org/10.1007/s11214-012-9908-y

McFadden, J. P., Carlson, C. W., Larson, D., Ludlam, M., Abiad, R., Elliott, B., … Angelopoulos, V. (2008). The THEMIS ESA plasma instrument and in-flight calibration. *Space Science Reviews*, *141*, 277–302.

Mende, S. B., Harris, S. E., Frey, H. U., Angelopoulos, V., Russell, C. T., Donovan, E., … Peticolas, L. M. (2008). The THEMIS array of ground-based observatories for the study of auroral substorms. *Space Science Reviews*, *141*, 357–387. https://doi.org/10.1007/s11214-008-9380-x

Murakami, G., Hirai, M., & Yoshikawa, I. (2007). The plasmapause response to the southward turning of the IMF derived from sequential EUV images. *Journal of Geophysical Research*, *112*, A06217. https://doi.org/10.1029/ 2006JA012174

Nishimura, Y., Lyons, L. R., Kikuchi, T., Angelopoulos, V., Donovan, E., Mende, S., … Nagatsuma, T. (2012). Formation of substorm Pi2: A coherent response to auroral streamers and currents. *Journal of Geophysical Research*, *117*, A09218. https://doi.org/10.1029/2012JA017889

Nosé, M., Liou, K., & Sutcliffe, P. R. (2008). Longitudinal dependence of characteristics of low-latitude Pi2 pulsations observed at Kakioka and Hermanus. *Earth Planets, and Space*, *58*, 775–783.

Nosé, M. (2010). Excitation mechanism of low-latitude Pi2 pulsations: Cavity mode resonance or BBF-driven process? *Journal of Geophysical Research*, *115*, A07221. https://doi.org/10.1029/2009JA015205

Onsager, T., Grubb, R., Kunches, J., Matheson, L., Speich, D., Zwickl, R. W., & Sauer, H. (1996). Operational uses of the GOES energetic particle detectors. In Washwell, E. R. (Ed.), *Society of Photo-Optical Instrumentation Engineers (SPIE) Conference Series* (Vol. 2812, pp. 281–290). Bellingham, WA: Society of Photo-Optical Instrumentation Engineers.

Osaki, H., Takahashi, K., Fukunishi, H., Nagatsuma, T., Oya, H., Matsuoka, A., & Milling, D. K. (1998). Pi2 pulsations observed from the Akebono satellite in the plasmasphere. *Journal of Geophysical Research*, *103*, 17,605–17,616.

Ream, J. B., Walker, R. J., Ashour-Abdalla, M., El-Alaoui, M., Wiltberger, M., Kivelson, M. G., & Goldstein, M. L. (2015). Propagation of Pi2 pulsations through the braking region in global MHD simulations. *Journal of Geophysical Research: Space Physics*, *120*, 10,574–10,591. https://doi.org/10.1002/2015JA021572

Redmon, R. J., Rodriguez, J. V., Green, J. C., Ober, D., Wilson, G., Knipp, D., … McGuire, R. (2015). Improved polar and geosynchronous satellite data sets available in common data format at the coordinated data analysis web. *Space Weather*, *13*, 254–256. https://doi.org/10.1002/2015SW001176

Rodriguez, J. V. (2014). GOES 13–15 MAGE/PD pitch angles algorithm theoretical basis document, version 1.0. Boulder, CO: NOAA National Geophysical Data Center. Retrieved from http://www.ngdc.noaa.gov/stp/satellite/goes/documentation.html

Ruohoniemi, J. M., & Baker, K. B. (1998). Large-scale imaging of high-latitude convection with super dual auroral radar network HF radar observations. *Journal of Geophysical Research*, *103*, 20,797–20,811.

Russell, C. T., Chi, P. J., Dearborn, D. J., Ge, Y. S., Kuo-Tiong, B., Means, J. D., … Snare, R. C. (2008). THEMIS ground-based magnetometers. *Space Science Reviews*, *141*, 389–412. https://doi.org/10.1007/s11214-008-9337-0

Shi, X., Baker, J. B. H., Ruohoniemi, J. M., Hartinger, M. D., Frissell, N. A., & Liu, J. (2017). Simultaneous space and ground-based observations of a plasmaspheric virtual resonance. *Journal of Geophysical Research: Space Physics*, *122*, 4190–4209. https://doi.org/10.1002/2016JA023583

Sibeck, D. G., & Angelopoulos, V. (2008). THEMIS science objectives and mission phases. *Space Science Reviews*, *141*, 35–59.

Singer, H., Matheson, L., Grubb, R., Newman, A., & Bouwer, D. (1996). Monitoring space weather with the GOES magnetometers. In Washwell, E. R. (Ed.), *Society of Photo-Optical Instrumentation Engineers (SPIE) Conference Series* (Vol. 2812, pp. 299–308). Bellingham, WA: Society of Photo-Optical Instrumentation Engineers.

Takahashi, K., Lee, D.-H., Nosé, M., Anderson, R. R., & Hughes, W. J. (2003). CRRES electric field study of the radial mode structure of Pi2 pulsations. *Journal of Geophysical Research*, *108*(A5), 1210. https://doi.org/10.1029/2002JA009761

Takahashi, K., Liou, K., Yumoto, K., Kitamura, K., Nosé, M., & Honary, F. (2005). Source of Pc4 pulsations observed on the nightside. *Journal of Geophysical Research*, *110*, A12207. https://doi.org/10.1029/2005JA011093

Takahashi, K., Berube, D., Lee, D.-H., Goldstein, J., Singer, H. J., Honary, F., & Moldwin, M. B. (2009). Possible evidence of virtual resonance in the dayside magnetosphere. *Journal of Geophysical Research*, *114*, A05206. https://doi.org/10.1029/2008JA013898

Takahashi, K., Bonnell, J., Glassmeier, K.-H., Angelopoulos, V., Singer, H. J., Chi, P. J., … Liu, W. (2010). Multipoint observation of fast mode waves trapped in the dayside plasmasphere. *Journal of Geophysical Research*, *115*, A12247. https://doi.org/10.1029/2010JA015956

Teramoto, M., Takahashi, K., Nosé, M., Lee, D.-H., & Sutcliffe, P. R. (2011). Pi2 pulsations in the inner magnetosphere simultaneously observed by the active magnetospheric particle tracer explorers/charge composition explorer and dynamics explorer 1 satellites. *Journal of Geophysical Research*, *116*, A07225. https://doi.org/10.1029/2010JA016199

Tsyganenko, N. A. (1989). A magnetospheric magnetic field model with a warped tail current sheet. *Planetary and Space Science*, *37*, 5–20.

Worthington, E. W., Sauter, E. A., & Love, J. J. (2009). Analysis of USGS one-second data. In Love, J. J. (Ed.), *Proc. XIII IAGA Workshop* (pp. 262–266). Golden, CO: United States Geological Survey.

Wygant, J. R., Bonnell, J. W., Goetz, K., Ergun, R. E., Mozer, F. S., Bale, S. D., … Tao, J. B. (2013). The electric field and waves instruments on the Radiation Belt Storm Probes mission. *Space Science Reviews*, *179*, 183–220. https://doi.org/10.1007/s11214-013-0013-7

Zou, S., Lyons, L. R., Wang, C.-P., Boudouridis, A., Ruohoniemi, J. M., Anderson, P. C., … Devlin, J. C. (2009). On the coupling between the Harang reversal evolution and substorm dynamics: A synthesis of SuperDARN, DMSP and IMAGE observations. *Journal of Geophysical Research*, *114*, A01205. https://doi.org/10.1029/2008JA013449

Zou, S., Lyons, L. R., Nicolls, M. J., Heinselman, C. J., & Mende, S. B. (2009). Nightside ionospheric electrodynamics associated with substorms: PFISR and THEMIS ASI observations. *Journal of Geophysical Research*, *114*, A12301. https://doi.org/10.1029/2009JA014259

Zou, S., Lyons, L., & Nishimura, Y. (2012). Mutual evolution of aurora and ionospheric electrodynamic features near the harang reversal during substorms. In Keiling, A., et al. (Eds.), *Auroral phenomenology and magnetospheric processes: Earth and other planets*. Washington DC: American Geophysical Union. https://doi.org/10.1029/2011GM001163